Chemical Engineering Science 65 (2010) 4983–4995

Contents lists available at ScienceDirect

Chemical Engineering Science

journal homepage: www.elsevier.com/locate/ces

Bulk video imaging based multivariate image analysis, process control chart and acoustic signal assisted nucleation detection

Levente L. Simon [a,*], Kaoutar Abbou Oucherif [b,1], Zoltan K. Nagy [c], Konrad Hungerbuhler [a]

[a] ETH Zurich, Institute of Chemical and Bioengineering, W. Pauli str. 10, Zurich 8093, Switzerland
[b] New-Mexico Institute of Technology, Department of Chemical Engineering, 801 Leroy Pl, Socorro, NM 87801, USA
[c] Loughborough University, Chemical Engineering Department, Loughborough LE11 3TU, UK

ARTICLE INFO

Article history:
Received 12 January 2010
Received in revised form
25 May 2010
Accepted 26 May 2010
Available online 1 June 2010

Keywords:
Crystallisation
Pharmaceuticals
Phase change
Slurries
Metastable zone
Image analysis

ABSTRACT

This article investigates monitoring technologies, which provide systematic solutions for nucleation detection based on external bulk video imaging (BVI). The methods under investigation rely on multivariate image analysis, image feature descriptors and statistical control charts (SPCs). For the design of SPCs the video information is transformed into time series. The application of SPCs may be hindered by autocorrelated time series, which show oscillatory patterns due to light reflections from the stirrer blades; however, the autocorrelation can be reduced by performing operations with the first principal component (*PC*1) of the captured color image or by stacking the frames based on the dominating frequency. Another option is to design digital signal filters in the frequency domain to decrease the autocorrelation of the time series.

It was found that the fastest methods for nucleation onset detection were the monitoring in the principal score space and control chart based monitoring of the mean gray intensity of the *PC*1 images sampled at 25 Hz. Furthermore, it was observed that performing principal component analysis (PCA) calculations on multidimensional or multispectral information not only provides the combination of variables that explain most of the variance at a certain time instance but also decreases the autocorrelation of the resulting time series.

For acoustic signal based monitoring the gray scale images were converted into a 2 channel stereo sound. It was found that this method has less performant nucleation onset detection capabilities compared to the methods which rely directly on the images.

1. Introduction

Crystallization is one of the most important unit operations in the pharmaceutical industry since it has the role of separation and purification, and it strongly influences the down-stream processing activities.

Metastable zone identification is the first step during the design of crystallization systems and is required to ensure reproducible crystal characteristics. Since the metastable zone width (MSZW) is not a thermodynamic property, it changes in function of several system characteristics such as: cooling rate, degree of stirring, solution history and presence of impurities or additives. The accurate determination of the metastable zone allows improved supersaturation control policies, ensures maximal productivity and the desired particle size distribution (PSD) at the end of the batch (Braatz, 2002; Nagy et al., 2008).

In order to determine the MSZW several sensors can be considered: turbidity (De Anda et al., 2005; Parsons et al., 2003), focused beam reflectance measurement (Fujiwara et al., 2002; O'Grady et al., 2007), spectroscopy (Anderson et al., 2001; Fujiwara et al., 2002; O'Grady et al., 2007; Pollanen et al., 2006), ultrasonic velocity measurements (Gurbuz and Ozdemir, 2003), density (Marciniak, 2002) and electrical conductivity monitoring (Lyczko et al., 2002), hot stage microscopy (Kumar et al., 1996), quartz crystal based monitoring (Joung et al., 2005; Loffelmann and Mersmann, 2002) and last but not least by visual inspection of the crystallizer content (Sohnel and Mullin, 1988). Kawabata et al. (2006) investigated imaging based nucleation onset and crystallization state monitoring for protein crystallization. The need for robust nucleation onset monitoring and prediction has been recognized by Pollanen et al. (2006) who proposed multivariate statistical process monitoring charts designed on the basis of IR spectra.

Recently, the proof of concept of bulk video imaging (BVI) was introduced to automate the nucleation detection by visual inspection. The particular feature of the noninvasive (Simon

* Corresponding author. Tel.: +41 44 6334486; fax: +41 44 6321189.
E-mail address: levente.simon@chem.ethz.ch (L.L. Simon).
[1] On research stay at ETH Zurich, Safety and Environmental Technology Group, now at Purdue University, USA.

0009-2509/$ - see front matter © 2010 Elsevier Ltd. All rights reserved.
doi:10.1016/j.ces.2010.05.045

et al., 2009a) or in situ (Simon et al., 2009b) BVI method is that it monitors the formation/dissolution of the solid phase using information from the bulk suspension providing a low-cost and automated method for MSZW determination, and making it a well-suited process analytical technology (PAT) method for the pharmaceutical and food industries. Moreover, the external BVI method can be considered as an external and non-contact matrix of turbidity probes. Previously, it was shown that BVI can be used for nucleation onset monitoring and metastable zone identification and has exhibited similar or better performance to the existing focused beam reflectance measurement (FBRM), ultra violet–visible (UV/Vis), infrared (IR) spectroscopy and calorimetric signals. In the previous work, one of the suggested image processing methods was to convert the colored images into gray scale and to calculate a mean gray intensity value. The nucleation onset was determined when the signal value rose above a threshold value, which was arbitrarily chosen. It has been recognized that the averaging operation filters the first particles, which are small and their contribution to the overall gray intensity is within the signal noise. The other proposed alternative, which is more complex from a design and an implementation point of view, suggests employing image processing techniques to detect the first crystals as objects (Simon et al., 2009b). Several other works related to image processing with application in the field of particulate technology focus on image segmentation for particle identification (Calderon De Anda et al., 2005; Eggers et al., 2008; Larsen and Rawlings, 2009; Larsen et al., 2006, 2007; Sarkar et al., 2009) while recent advances for the 3D characterization are also reported (Darakis et al., 2010; Khanam et al., 2008; Kempkes et al., 2009; Kempkes et al., 2010).

Turbidity based nucleation detection is a widespread approach for nucleation detection; however, it is an in situ hence invasive detection method. The external BVI provides good nucleation detection while the probe is placed externally; hence, cleaning, contamination and sensor fouling related problems are eliminated. Since the BVI method relies on a video signal, the aim of this work is to investigate monitoring technologies, which provide systematic, sensitive and robust solutions for nucleation detection. To achieve these goals, video signal sampling alternatives and image processing techniques such as multivariate image analysis (MIA) and image feature descriptors are evaluated. The multivariate image analysis method is selected because of the multispectral nature of color pictures while feature descriptors are considered due to their low level of computational complexity. It is proposed that whenever feasible, the time series trends generated using the methods mentioned above are monitored using Shewhart and EWMA statistical control charts to provide systematic nucleation onset detection. An alternative monitoring method based on acoustic features is proposed by transforming the video images into stereo sound signals. To the authors' knowledge, it is for the first time that the problem of systematic nucleation onset detection is tackled using multivariate image analysis.

The article is structured as follows: after the description of the motivation and experimental setup, the monitoring techniques are introduced and discussed. The results and discussion section presents the evaluation results and highlights the advantages of each method. An overall comparison of the proposed methods and final conclusions are presented in the last section.

2. Experimental

The external BVI method is based on recording the crystallization process with a video camera, which captures 25 frames per second. The video camera is placed externally and the crystallizer vessel is covered with black folia in order to ensure a dark background. The speed of the stirrer with four pitched blades was fixed at 100 RPM. For large scale applications the camera can be used through an observation window. The illumination conditions are similar to those found in industrial crystallizers where the illumination of the liquid bulk is low. Anhydrous caffeine from Sigma-Aldrich with a minimum purity of 98% in deionized water was used as the model. Details of the experimental setup are found in previous work (Simon et al., 2009a).

3. Bulk video imaging based nucleation monitoring

In this work several video data sampling and image processing technologies are evaluated to provide a robust and sensitive solution for systematic nucleation detection, as shown in Fig. 1. The first class is the multivariate image analysis (MIA) framework based on statistical concepts. Multivariate image analysis methods decompose color red–green–blue (RGB) images into principal components, which are also images. Within the class of MIA, the monitoring in the score space of the original RGB image and the PCA model prediction error monitoring techniques are implemented. The second class relies on feature descriptors while the third method converts the video information into a stereo sound.

3.1. Video data sampling and preprocessing

Previously it was observed that the time series trends of the average of gray scale images show oscillatory patterns (Simon et al., 2009a, b) while detailed investigation has shown that these oscillations of the image luminosity are due to the light reflected by the stirrer blades. By performing an analysis of the time series data in the frequency domain, several oscillation patterns are revealed as shown by the power density plot in Fig. 2. These oscillating patterns hinder the application of control charts; therefore, one has to design a digital signal filter for the time series or has to perform the image sampling in such a way that the pattern is removed. Such a filter is the notch filter, which is a band-stop filter with a narrow stop band that passes most frequencies unaltered, but attenuates those in a specific range to very low levels.

The dominating frequencies found in the trends are due to the stirrer rotation, which was fixed at 100 RPM and corresponds to 1.66 Hz. Although the blades of the stirrer are similar and one could expect the dominating frequency at four times the stirrer speed (6.6 Hz), it is believed that the peak at 1.66 Hz is due to the oscillation of the entire stirrer along the horizontal position.

The video information sources are the RGB color images of $M \times N \times 3$ dimensions, which are defined by the stacked R, G and B color channels:

$$RGB = \{R,G,B\} \tag{1}$$

where M is the image width [pixels], N is the height [pixels], R, G, and B are sets of pixels belonging to the red, green and blue color components

$$R = \left\{x_1^R, x_2^R, \ldots, x_q^R, \ldots, x_{MN}^R\right\},\ G = \left\{x_1^G, x_2^G, \ldots, x_q^G, \ldots, x_{MN}^G\right\},$$
$$B = \left\{x_1^B, x_2^B, \ldots, x_q^B, \ldots, x_{MN}^B\right\} \tag{2}$$

where x_i^R, x_i^G, x_i^B are the intensity values of color pixels in the image.

The video signal sampling strategy can influence the nucleation onset monitoring performance; therefore, this work evaluates several sampling strategies. The first sampling method considers calculations on each frame (25 Hz frequency). According to the second method calculations are performed by

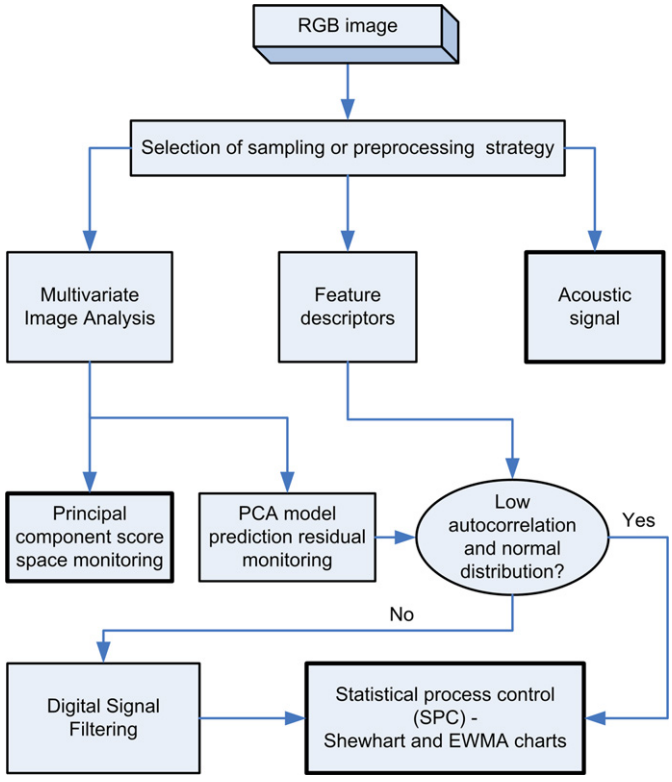

Fig. 1. Schematic representation of the nucleation onset monitoring methods.

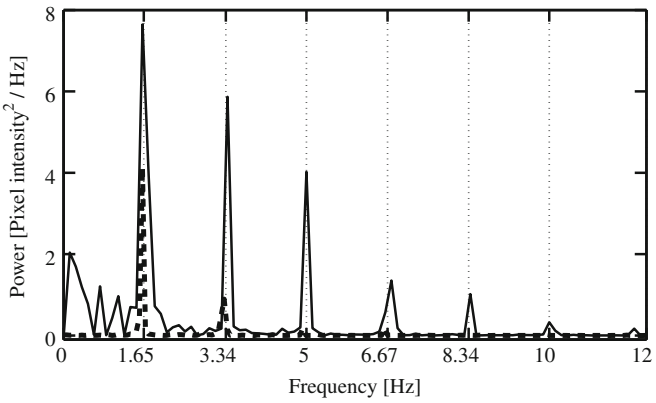

Fig. 2. Power density plot of the mean gray trend using 25 Hz sampling for two different experiments.

overlapping the images to increase the particle density. Stacked information is also used within the framework of multiway PCA/PLS methods to represent the process parameter values during batch process monitoring (Nomikos and MacGregor, 1994, 1995a). Hereafter stacking, the overlapping operation is carried out resulting in a single image. Information stacking is also specific to the repetitive and run-to-run control strategies (Wang et al., 2009). The overlapping method can also be applied to the gray and first principal component images; the calculation of these is discussed in the follow-up sections. To overlap 15 frames, the *R*, *G* and *B* channels are extracted individually from each frame then stacked to form an $M \times N \times 15$ matrix. The number of frames to be overlapped should be determined according to the dominating frequency, e.g. 1.66 Hz for this case. For the *PC1* images a PCA calculation is required before stacking. The result of stacking is an $M \times N$ matrix which is obtained by retaining the maximum intensity value along the 3rd dimension

$$\overline{\overline{Ch}}_{n,m} = \max_{f\,=\,1..25} (Ch_{n,m,f})\ n = 1,\ldots,N;\ m = 1,\ldots,M;\ Ch \in \{R,G,B,GR,PC1\} \quad (3)$$

where $\overline{\overline{Ch}}$ represents the *R*, *G*, *B*, gray (*GR*) or *PC*1 channel of 15 overlapped frames and it is a two dimensional matrix. The result of the overlapping operation is an RGB image which contains all particles encountered in one of the 15 frames. The overlapping method is similar to the addition operation often used in image processing. Unlike the addition operation along the pixels where the intensities saturate above 255 and re-normalization is needed, when the overlapping method is used, the pixel values are always in the 0–255 range. It is expected that this method will decrease the autocorrelation of the time series since it performs an operation along the frames.

3.2. Multivariate image analysis

The multivariate image analysis based nucleation monitoring strategy is justified by the fact that the captured frames consist of three color channels; hence, these are multispectral. Low-cost video cameras use a single light sensitive sensor and a color filter array (CFA) with each pixel unit recording the intensity value of each color channel typically red, green and blue. The most widespread CFA is the Bayer filter (Bayer, 1976) shown in Fig. 3. In this scheme the green filters are in a quincunx – interlaced – grid with the red and blue completing the rest of the empty cells. Note that the CFA captures only one-third of the needed color intensities and it provides a 2D color matrix. Furthermore, the green color filters make up half of the cells while the rest is shared by the blue and red filters. This is due to the fact that the luminance response curve of the eye peaks at around the frequency of green light. As a next step, this 2D structure is converted into the well known 3D or RGB color format by an interpolation method. This process is

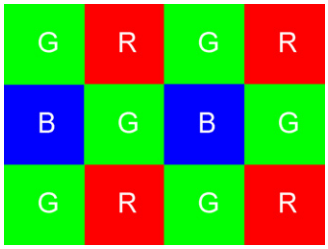

Fig. 3. The Bayer filter (Bayer, 1976).

called debayering or demosacking. Some of the interpolation methods are nearest neighborhood, bilinear interpolation, smooth hue transition, adaptive color plane interpolation and gradient based interpolation (Ramanath et al., 2002).

One source of correlation might be due to the fact that only every third pixel value is a true measurement and the rest of the pixel values are obtained by interpolation. Furthermore, image compression algorithms may introduce additional correlation among the color channels; therefore, multivariate image analysis has been proposed to compress and extract uncorrelated information using multiway principal component analysis (Geladi et al., 1989). MPCA decomposes the unfolded multivariate image array U into principal components made of score matrices t_a, loading vectors p_a and into a residual matrix E:

$$U = \sum_{a=1}^{A} t_a p_a^T + E \tag{4}$$

where A is the number of principal components. The multiway PCA implementation proposed for the nucleation onset monitoring follows the methodology described in previous works (Bharati and MacGregor, 1998; Geladi et al., 1989) and the loading vectors are computed using the efficient kernel algorithm proposed by Geladi et al. (1989). The kernel matrix (U^TU) is first constructed and a singular value decomposition (SVD) is performed on the matrix to extract the loading vectors p_a and the corresponding score vectors t_a are calculated according to Eq. (5):

$$t_a = Up_a \tag{5}$$

The calculation results have been validated against the results provided by the MACCMIA Matlab tool (Dunn, 2007) developed at McMaster University, Canada. Several MIA based applications in the context of process engineering have been reported: online monitoring of snack food processes (Yu and MacGregor, 2003; Yu et al., 2003), flames monitoring (Szatvanyi et al., 2006; Yu and MacGregor, 2004), flotation froth monitoring (Liu et al., 2005), anode cover alumina content (Tessier et al., 2008) and mineral ore composition estimation (Tessier et al., 2007), counterfeit drug detection (Rodionova et al., 2005), emulsion monitoring (de Juan et al., 2005, 2008), quality control of polymer blends (Gosselin et al., 2009), semiconductor characteristics monitoring (Facco et al., 2009) and recently crystal (Sarkar et al., 2009) and fiber size distribution determination (Tomba et al., 2010).

3.2.1. PCA model prediction error monitoring

Within the context of MIA, another alternative is to monitor the PCA model prediction error. As the PCA model is built on images containing crystal clear solution, upon nucleation, new features appear in the images. These features, which were not considered by the PCA model, will lead to the increase of the sum-of-squares prediction error. In case the time series trend of the PCA model prediction error is normally distributed and auto-correlation is low, a SPC can be built. Alternatively, a threshold value can be set to trigger the alarm for the nucleation onset. Depending on the degree of explanation, the first or first two principal components can be used for prediction. In this work PCA is carried out simultaneously on 15 frames (corresponds to the dominating frequency of 1.66 Hz) arranged in a single $(15N \times M \times 3)$ matrix. This way the autocorrelation of the time series should be decreased.

3.2.2. PCA score space based monitoring for infrequent events

According to this method, a PCA model is built on images which contain only common case variation as discussed by Bharati and MacGregor (1998). For nucleation onset monitoring purposes, the state of normal operation is represented by the clear liquid without crystals while the crystals appearing in the liquid are considered as infrequent special events.

According to Bharati and MacGregor (1998) a mask that defines the pixels belonging to crystals is defined in the score space of the first two principal components and the number of pixels is counted off-line. It is expected that upon nucleation the number of pixels falling within the mask boundaries matches the number of pre-observed pixels within a certain tolerance; otherwise, it is concluded that crystals are not present. A threshold value on the number of pixels falling under the mask can be set and used to detect nucleation. A score space based monitoring application has been presented by Bharati et al. (2003) for the monitoring of lumber defects.

3.3. Feature descriptors

Feature descriptors are used to represent information for a certain group of pixels and in this work they are considered due to their calculation simplicity. Global feature descriptors such as the average color or the loading of the first principal component have been used for the monitoring and prediction of coating content in the snack industry (Yu and MacGregor, 2003). Furthermore, uniformity of brightness and average brightness features of different regions of the score space have been selected for the monitoring of flames (Yu and MacGregor, 2004). Zhou et al. (2009) proposed the intensity range to detect whether a particle is present in the image acquired with a particle video microscope (PVM) unit. The main characteristic of the previous descriptors is that they do not retain spatial features and relationships among the pixels. To overcome this drawback Sarkar et al. (2009) used several spatial descriptors to identify crystals in a crystallization process. More complex feature descriptors are used for image texture analysis (Bharati et al., 2004).

In this work, for the purpose of nucleation onset detection the average descriptor is used; furthermore, since the crystals which are formed are brighter than the image background the maximum intensity descriptor is additionally introduced. The conversion of RGB images to gray scale (GR) is performed by the weighted summation of the R, G and B components:

$$Gr_{n,m} = 0.2989R_{n,m} + 0.5870G_{n,m} + 0.1140B_{n,m} \tag{6}$$

The obtained gray scale represents the luminance of the original image and the weights in Eq. (6) are derived from the NTSC-standard (National Television System Committee) used for analog television signals. The mean intensity of each channel is defined as follows:

$$\overline{Ch} = \frac{\sum_{q=1}^{MN} x_q^{Ch}}{MN} \quad Ch \in \{R,G,B,GR,PC1\} \tag{7}$$

$\overline{Ch}$ represents the mean of red, green, blue, gray and $PC1$ images and it is a scalar. The maximum intensity of the RGB image $RGB_{\max}$ is defined as

$$RGB_{\max} = \max(\max(R),\max(G),\max(B)) \tag{8}$$

These descriptors can be calculated over an *RGB* image, separate *R*, *G*, *B* channels, gray scale images or principal component scores resulting from the multivariate image analysis. Since it is not the purpose of this work to detect boundaries, spatial descriptors are not considered. Furthermore, it is important to assess the time series trends generated by the feature descriptors with respect to normality and autocorrelation as these will be used to design Shewhart and EWMA process monitoring charts.

3.4. Statistical process control using univariate Shewhart and EWMA charts

Statistical process control charts are efficient and established tools for process monitoring. Control chart assisted monitoring has been applied to nucleation detection using IR spectroscopy (Pollanen et al., 2006). Furthermore, a control chart and vision-based process monitoring of metallic surfaces was presented by Armingol et al. (2003). The authors proposed a multivariate control chart for the monitoring of pixel values within an observation window, and an out-of-control signal is generated if any of the pixel values are outside of the control interval. An EWMA based intensity value forecasting and residual monitoring approach was presented by Nembhard et al. (2003) for the transition monitoring of a plastic extrusion process.

The fundamental assumption behind the traditional control charts is that the time series contains independent random variables. Deviation from the assumption of low autocorrelation yields the decrease of the in-control average run length leading to higher false alarm rates. To investigate the autocorrelation patterns in the frequency domain frequency plots or period-ograms are used and the autocorrelation extent is evaluated by using autocorrelation charts. More information on autocorrelation is given in Appendix A.

The second requirement to build a control chart is that the data should be normally distributed around the mean. In this work, normality is assessed by using data histograms and is quantified by the Lillefors test (Lilliefors, 1967). The Lilliefors test is a two-sided goodness-of-fit test suitable when a fully-specified null distribution is unknown and its parameters must be estimated. The default null hypothesis is that the sample comes from a distribution in the normal family, against the alternative that it does not come from a normal distribution.

The monitoring robustness of Shewhart and EWMA charts is increased by introducing the following rules: 5 or 10 chart points should be consecutively out of control; this control rule introduces at least $5ng/fs$ seconds delay, where ng is the sub-group size and fs [Hz] is the sampling frequency. The nucleation onset monitoring in a stirred vessel using image analysis is prone to generate an autocorrelated signal with oscillating patterns due to the light reflected from the blades of the stirrer. Attempts to decrease the autocorrelation in the time series trends can be made by using a digital filter designed based on frequency plots. All the time series in this work are subject to autocorrelation and normality tests with a 3σ confidence interval.

3.5. Digital signal filtering

The aim of this section is to provide a short description to digital filter design and for more details the reader is referred to the literature (Oppenheim and Schafer, 2010). The filters designed in this work are given by Eq. (9) and are based on the Blackman window:

$$F(i) = K\frac{\sin(2\pi f_c(i-H/2)}{i-H/2}\left[0.42-0.5\cos(2\pi i/H)+0.08\cos(4\pi i/H)\right]$$

$$\text{for } i = H/2,\ F(i) = 2\pi f_c \tag{9}$$

where F is the filter value, K is a constant, f_c is the cutoff frequency expressed as the fraction of the sampling rate and H is the size of the filter kernel.

In order to obtain a band-reject or band-stop filter two low-pass filters are designed using Eq. (9). A high-pass filter is obtained by performing a spectral inversion of the low-pass filter with highest cutoff frequency. The band-reject filter is obtained by adding the low-pass and high-pass filters. Similar to the procedure mentioned above 7 band-reject filters are designed to remove the oscillations from the data, Fig. 4a. The filter kernel size is 1000 points in order to obtain good roll-off properties (filter behaves similarly to an ideal filter).

According to Fig. 2, it is observed that the dominating frequencies occur at intervals of 1.66 Hz; therefore, a moving average filter could also be considered since these have low-pass filtering characteristics. The size of the window is set by the highest dominating frequency, which is 1.66 Hz and corresponds to 15 mean gray intensity values. The frequency response of a moving average filter with 15 points is given by Eq. (10) and is presented in Fig. 4b.

$$F(fr) = \sin(\pi frW)/W\sin(\pi fr) \tag{10}$$

where fr is the frequency value expressed as the fraction of the sampling rate and W is the size of the moving window.

3.6. Image transformation into acoustic signal

The transformation of measurement data into acoustic signals provides alternative monitoring solutions. The acoustic monitoring performance for nucleation onset detection has been investigated using the acquired video frames. According to this method the RGB frames are first converted to gray scale images. Each gray image is then divided to two equal 2D images along the width, and the matrices were unfolded into vectors. As a result two $MN/2$ vectors are obtained corresponding to a stereo sound signal. The playback sampling frequency is $25MN/2$ Hz. The signals are scaled between -1 and 1 a priori to avoid clipping. The scaling was performed by specifying a minimum and a maximum value to map all the data points in the full sound range. The maximum value was set around a value where nucleation onset has already occurred. Note that typical computer soundcards support sampling frequencies between 5 and 44.1 kHz; therefore, some of the image pixel values might need to be

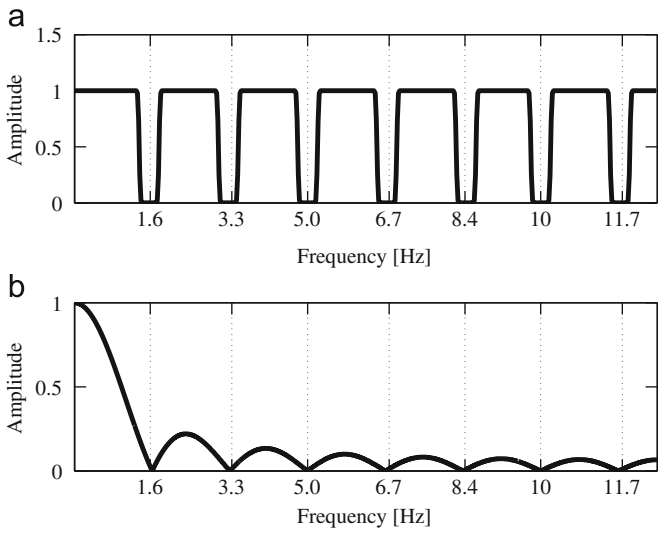

Fig. 4. The band-stop (a) and a 15 point moving average (b) filter response in the frequency domain.

discarded. According to the maximum sampling frequency for nucleation monitoring purposes an unfolded image with $2 \times 44\,100$ pixels can be used to obtain a stereo sound.

The following Matlab (The Mathworks, 2009) toolboxes were used within this project: Image Processing Toolbox, Signal Processing Toolbox, Statistical Toolbox, Time Series Analysis Tool and MACCMIA (Dunn, 2007) multivariate image analysis package.

4. Results and discussion

For plotting purposes the experimental data is presented about 10–15 min prior to nucleation. In order to provide an accurate evaluation of the monitoring performance, a visual investigation of the video data was performed and the frame-by-frame analysis has shown that the first crystal appears after 784 s. Note that this crystal was not visible when the video was played at 25 frames/s; therefore, by observing the liquid phase early crystal detection by visual means is not feasible. The result of the overlapping operation is presented in Fig. 5, where it is observed that all particles which are present in the individual frames are found in the overlapped frame and the overall picture brightness has increased. This operation can also be considered as a method to concentrate the information acquired in several frames.

4.1. Multivariate image analysis

Upon the application of multiway PCA to an RGB image, three principal components are obtained. Typical loading values of images without crystals for the two monitoring methods are presented in Table 1. The first score is a linear combination of the three color channels, and it can be considered as a method to convert a color image to a gray scale based on statistical principles. Similar to the mean gray intensity, a mean value of the first principal component can also be calculated.

The complements of the three principal components of an image taken by the external camera are shown in Fig. 6. The first principal component contains most of the information while the second and the third components contain mostly noise. This observation is confirmed by the sum of square explained values of the principal components presented in Table 1.

4.1.1. PCA model based monitoring

The results of the PCA model prediction error trend using Shewhart and EWMA charts are shown in Fig. 7a. Throughout this work, the gray line represents the Shewhart chart while the black corresponds to the EWMA chart. The PC model was built using clear liquid images and only the first principal component was used for prediction.

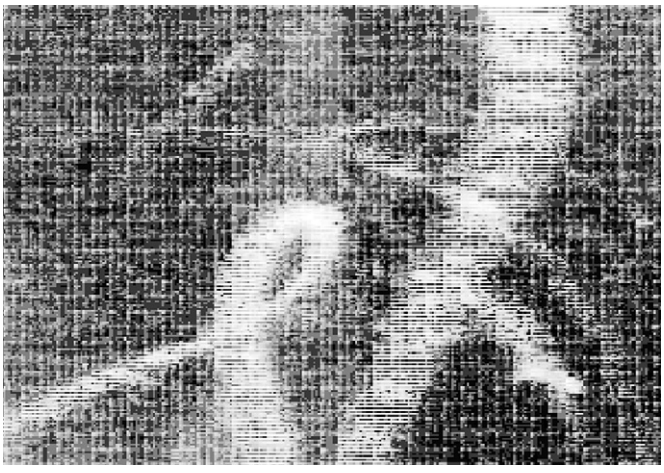

Fig. 5. Result of the overlapping operation: 25 gray scale images overlapped (the image is contrast enhanced by histogram equalization for visualization purposes).

Table 1
Principal components loadings and sum of squares explained for the BVI data.

	Loading vectors			Sum of squares explained (%)
p_1^T	−0.605	−0.547	−0.578	98.88
p_2^T	0.374	0.445	−0.813	0.78
p_1^T	0.703	−0.708	−0.065	0.44

The PCA modeling residual trend for the 25 Hz sampling has shown the same correlation pattern as the mean gray trend with the same dominating frequencies; therefore, a statistical process control chart was not designed. Instead, the error trend obtained by performing a PCA prediction on 15 stacked frames which passed both the autocorrelation (Fig. 7b) and normality tests and it was used for nucleation detection. The Shewhart-5 chart detected the nucleation at 1045 s which is 261 s later than by the frame-by-frame analysis. The EWMA-5 and EWMA-10 charts detected the nucleation at 974 and 980 s. Throughout this work a memory factor of 0.4 was used in the EWMA calculations. Note that the EWMA chart, using the same detection rules as the Shewhart chart, is faster at detecting the crystals due to its memory effect.

4.1.2. PCA score space based monitoring for infrequent events

For this monitoring strategy the number of frames to be stacked is arbitrary. A stacking of 25 frames was implemented to increase the particle concentration in the overlapped image. The score plots of *PC*1 versus *PC*2 of images with crystals, using two different sampling methods at 25 Hz without and with overlapping are shown in Fig. 8a and b, respectively. The corresponding first principal component images are presented in Fig. 9a and b, respectively. The pattern corresponding to crystals is found at the highest intensity values. For single images, it is observed that the pattern is less well defined than for 25 frames overlapped. Also note that the contrast of *PC*1 images varies.

In order to determine the mask which contains the pixels corresponding to crystals the MACCMIA Matlab tool (Dunn, 2007) is used. Cropped snapshots of the tool and score mask for the 25 Hz overlapped sampling strategy are shown in Figs. 10 and 11. It is observed that the crystals can be easily identified in the score space. Furthermore, it is concluded that monitoring only based on the *PC*1 score is enough. Therefore, *PC*1 score intervals are identified within which the pixels correspond to crystals. Note that the position of the score plot is different compared to Fig. 8a and b, although the score pattern is the same. This is due to the application of the image complement operator, which converts dark pixels into bright ones and bright pixels are converted to dark.

The score space of a single image sampled at 25 Hz is shown in Fig. 11, and it is concluded that also single crystals can be identified in the score space.

For a proper tuning of the score interval, a sensitivity analysis is carried out. Note that the number of pixels falling under the mask for the 25 Hz overlapped strategy is higher since it concentrates the information gathered during 1 s. The monitoring results of the number of pixels contained in the score mask are shown in Figs. 12 and 13 for the 25 Hz overlapped and 25 Hz sampling with no overlapping, respectively. It is considered that crystals are present when the number of pixels is below 1000 for the 25 Hz overlapped sampling strategy and below 200 pixels

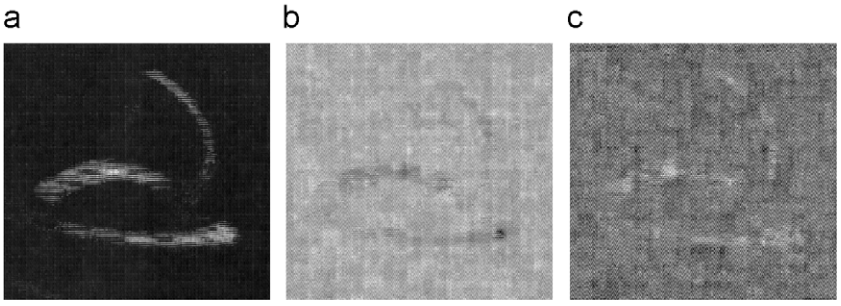

Fig. 6. The complements of PCA scores of an overlapped image: (a) *PC*1, white traces show the moving crystal trajectory, (b) *PC*2 and (c) *PC*3.

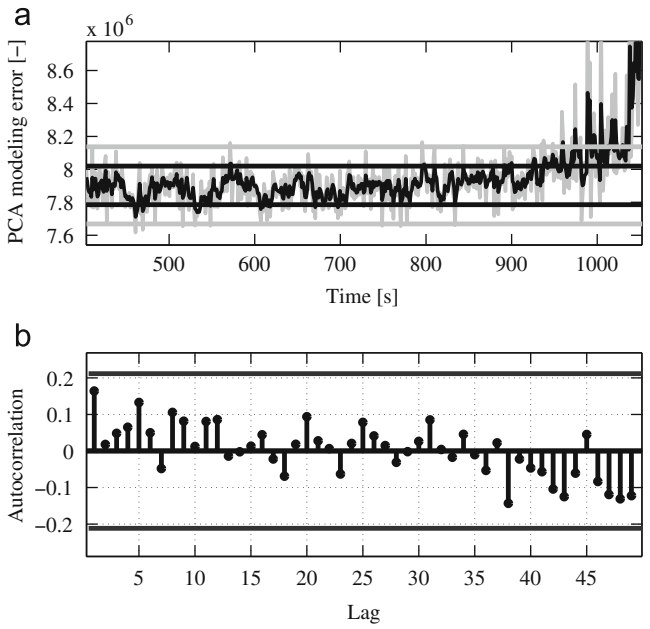

Fig. 7. PCA modeling error trend based on *PC*1 (a) and the autocorrelation chart (b).

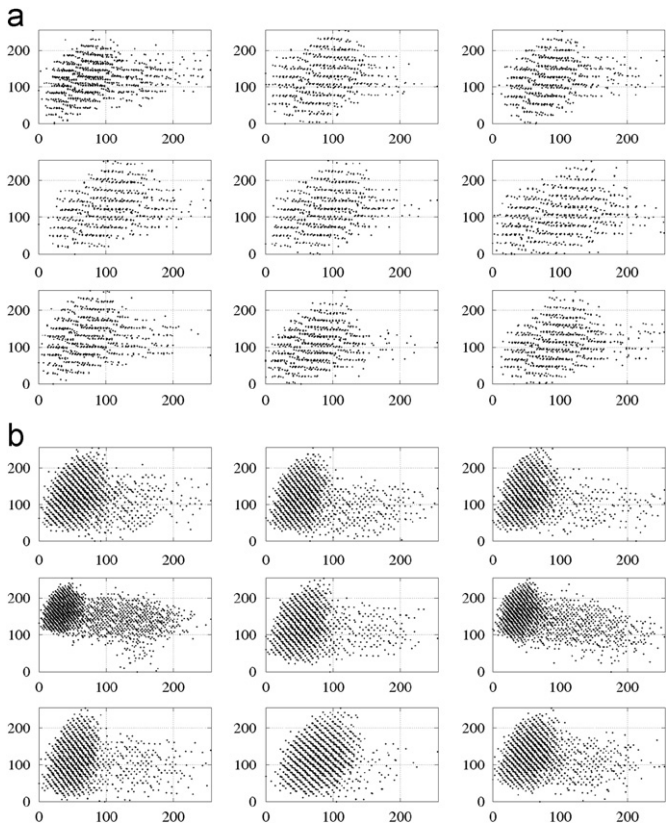

Fig. 8. *PC*1 versus *PC*2 score space plots of BVI images containing crystals sampled at 25 Hz no overlapping (a) and 25 Hz with overlapping (b).

for the 25 Hz sampling. It is observed that for the 25 Hz with overlapping sampling there are few false alarms and the nucleation detection is after 852 s. The same conclusions are drawn for the 25 Hz sampling with no overlapping case where nucleation is detected slightly earlier, after 841 s; however, the number of false alarms also increased. For all cases it is required that at least 5 positive matches are within 1 s.

4.2. Feature descriptors

The comparison of mean gray and RGB_{max} trends is shown in Fig. 14.

Relying on visual analysis, it is concluded that the RGB_{max} index is the first to show the presence of crystals since no averaging operation is performed. The large detection difference between the mean gray and RGB_{max} trends is due to the large monitoring window compared to the small particles. Note that the mean of overlapped trends is about 5 intensity units larger since the overlapping operation takes the maximum pixel value along 25 frames. In this video data the size of a crystal is about 130 pixels, while the interrogation window contains 72 900 pixels corresponding to a size of 300×243. In Table 2 the results of the autocorrelation, normality and detection results are summarized.

The frame-by-frame sampling produced highly correlated trends with partial fulfillment of the normality criterion. Only the trends which passed both tests were considered for monitoring. It is interesting to note that the *PC*1 trend successfully passed both tests and the detection performance was good compared to the visual crystal detection. The time series trend of *PC*1 is less autocorrelated due to the *RGB*-to-gray conversion weights, which change dynamically according to the input image and are the result of the SVD calculation. The autocorrelation chart and the frequency response of the signal used to build the SPC are shown in Fig. 15, while the control chart is presented in Fig. 16.

For this video data, overlapping 15 frames followed by calculating the mean of the image did not result in time series, which could be used to build SPCs (Table 2b). A systematic feature of the time series obtained by taking the maximum value in a frame (including frames obtained by overlapping, Table 2c) is that

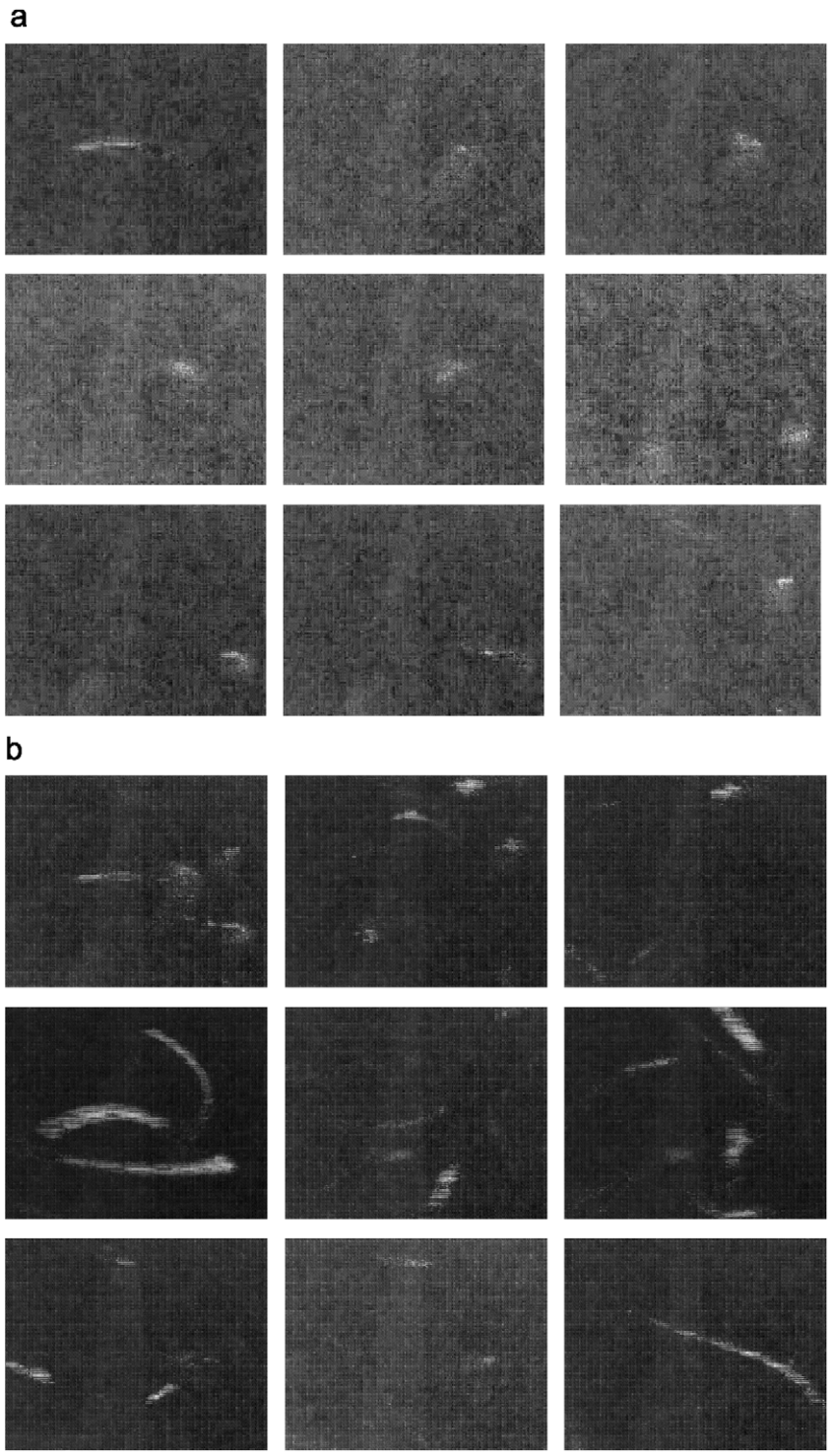

Fig. 9. The *PC*1 images containing crystals sampled at 25 Hz no overlapping (a), and 25 Hz with overlapping (b) corresponding to the score plots in Fig. 8a and b.

these are not autocorrelated and the normality requirement is violated marginally for some cases. Although none of the time series passed the normality test at 3σ, they still show monitoring potential.

By computing the mean of 25 frames (Table 2d), the autocorrelation is not removed, the detection performance is poor, and early false alarms are generated. The averaging over 25 frames for the *PC*1 signal yields a non-autocorrelated trend. The mean *R*, *G*, *B* and *GR* trends of 25 overlapped frames are autocorrelated and this operation introduces a detection delay of about 80 s compared to the 25 Hz sampling.

The autocorrelation chart is presented in Fig. 17a where it is observed that the autocorrelation coefficients are located within the 3σ confidence band and no particular patterns can be identified. The Shewhart (gray) and EWMA (black) charts of the same trends are shown in Fig. 17b.

The decreasing trend of the *PC*1 signal upon nucleation was observed in all BVI trends, which relied on the averaging of the

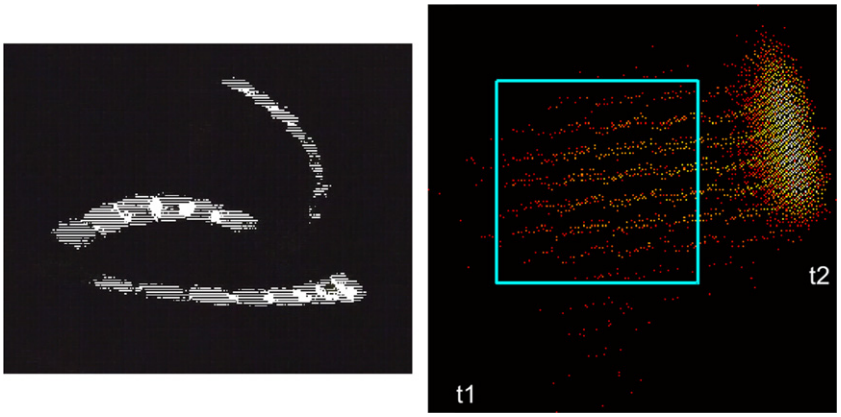

Fig. 10. Cropped snapshots of the MACCMIA tool used for mask position determination. Pixels under the mask in the score space (a) corresponding to crystals (b); the sampling is at 25 Hz with overlapping; mask size is 128 × 128 pixels and the number of pixels under the mask is 3500.

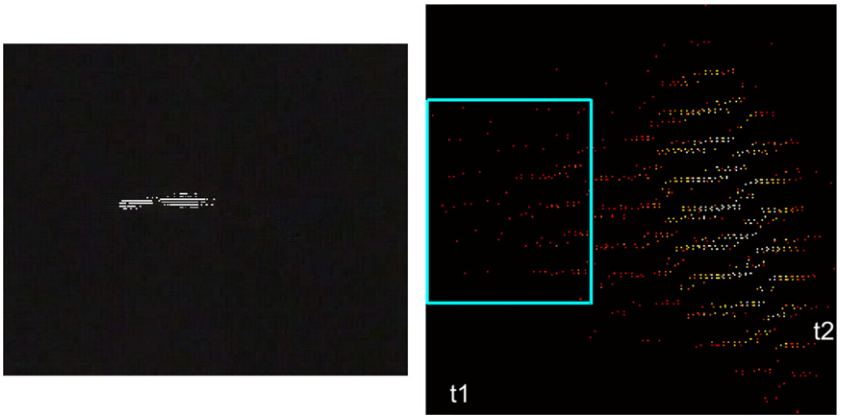

Fig. 11. Cropped snapshot of the MACCMIA tool used for mask position determination. Pixels under the mask in the score space (a) corresponding to a single crystal (b); 25 Hz sampling, no overlapping. The mask size is 100 × 128 pixels and the number of pixels under the mask is 200.

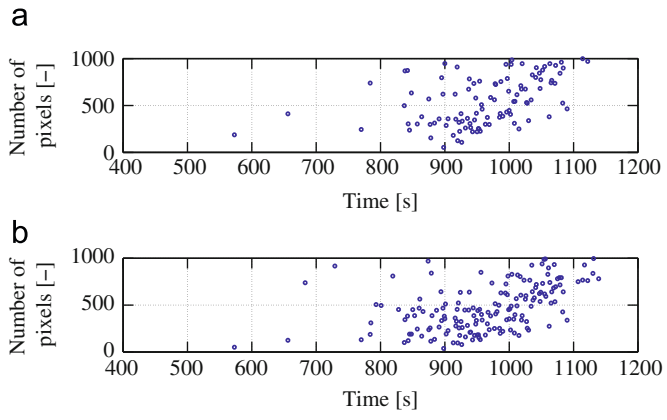

Fig. 12. Number of pixels falling within the 144–255 (a) and 154–255 (b) interval of the 1st *PC* score for the 25 Hz with overlapping sampling. Nucleation detection at 852 and 854 s, respectively.

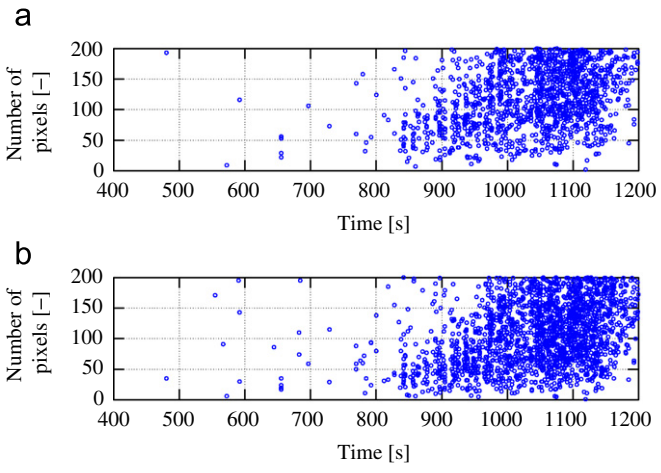

Fig. 13. Number of pixels falling within the 105–255 (a) and 115–255 (b) interval of the 1st *PC* score for the 25 Hz without overlapping sampling. Nucleation detection at 841 s in both cases.

*PC*1 images. Note that the loading vector is negative and in order to perform a gray scale conversion, the image complement operator has to be applied according to which dark pixels become bright and vice versa. In the resulting *PC*1 image the crystals are white and the background is dark. Detailed inspection of the *PC*1 images shows that upon nucleation the background becomes darker than the clear liquid *PC*1 background, which is why the mean gray intensity trend decreases. Upon nucleation of a large amount of crystals the mean intensity trend increases again. The 1 Hz sampling (Table 2e) yields an autocorrelated signal and it was found that also for this case working with the mean of *PC*1 yields a signal that can be used for SPC based monitoring.

Based on the results discussed above it is concluded that performing PCA calculations on multidimensional or multispectral information not only provides the combination of variables that explain most of the variance at a certain time instance but

also decreases possible autocorrelation features of the resulting time series.

In order to decrease the autocorrelation of the time series, a sampling time corresponding to 1.66 Hz or every 15 th frame was also implemented. Although this strategy removed all the high frequency correlations, oscillations at lower frequencies resulted in autocorrelated trends and rendered the application of SPCs unfeasible. The oscillations at low frequencies might be due to the cooling agent, which is circulating in the jacket. This sampling strategy might give good results when the images are directly taken from the bulk using an endoscope or through an observation window. Another sampling strategy that failed the autocorrelation test was the averaging of gray intensity points by blocks of 15 values. This operation resulted in a signal with oscillations having frequencies lower than 1.66 Hz.

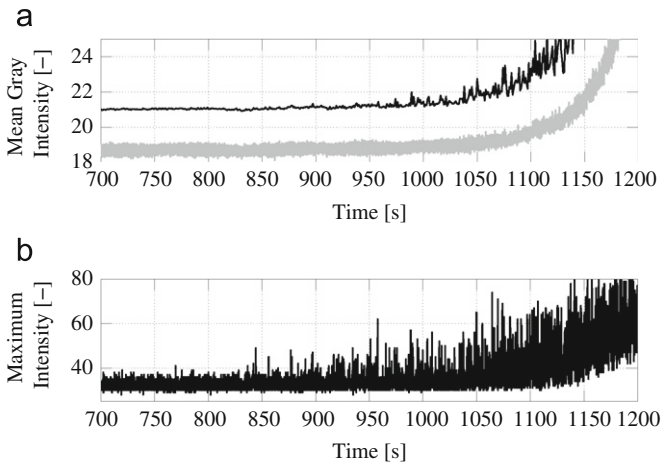

Fig. 14. Feature descriptor trends: (a) mean gray intensity trends at 25 Hz sampling (gray) and 25 Hz sampling with overlapping (black), (b) the RGB_{max} trend at 25 Hz sampling.

Another set of observations are related to the standard deviations of the mean *R*, *G* and *B* trends calculated for 300 data points for a clear liquid. The standard deviations are as follows: red 0.456, green 0.145 and blue 0.534. It is concluded that the green channel has the highest signal to noise ratio; note that green makes up for the half of the Bayer matrix elements. Still, explaining the low standard deviation value with the filter structure might be difficult as the analyzed images have already suffered a compression using an MPEG2 (Moving Pictures Expert Group) encoding and the measured values have been changed. Alternative methods for nucleation detection based on digital images are the employment of artificial intelligence techniques for pattern matching (Simon and Hungerbuhler, 2010).

4.3. Digital filtering results

In order to remove the autocorrelation the band-stop digital filters (Fig. 4) based on the Blackman window were applied. The resulting signal in the frequency domain is shown in Fig. 18a, while the results for the moving average filter are shown in Fig. 18b. As it is observed in both plots, the dominating frequencies were successfully removed; however, other low frequency oscillation patterns are still detected. These patterns hinder the application of SPCs in both cases as the signal shows non-normal distribution and high autocorrelation. The removal of dominating frequencies due to the stirrer rotation is not enough for control chart based monitoring since low-frequency oscillations are still found in the data. As mentioned before, it is thought that these oscillations are due to the circulating cooling liquid in the jacket. It is concluded that the frequency response of

Table 2
Summary of feature descriptor trends detection performance. First visually detected crystal is at 784 s.

Sampling method	Feature descriptor	Autocorrelation test	Normality test	Detection time (s)		
				Shewhart-5	EWMA-5	EWMA-10
(a)	RGB_{max} (Fig. 14b)	OK	X	–	–	–
25 Hz	Mean gray (Fig. 14a)	X	X	–	–	–
	Mean red	X	X	–	–	–
	Mean green	X	X	–	–	–
	Mean blue	X	X	–	–	–
	Mean *PC*1 (Fig. 15a and b, Fig. 16)	OK	OK	897	842	842
(b)	RGB_{max}	OK	X	–	–	–
15 overlapped frames	Mean gray	X	OK	–	–	–
	Mean red	X	OK	–	–	–
	Mean green	X	OK	–	–	–
	Mean blue	X	OK	–	–	–
	Mean *PC*1	X	OK	–	–	–
(c)	$Gray_{max}$	OK	X	–	–	–
15 overlapped frames	Red_{max}	OK	X	–	–	–
	$Green_{max}$	OK	X	–	–	–
	$Blue_{max}$	OK	X	–	–	–
(d)	Mean gray (Fig. 14a)	X	OK	–	–	–
25 overlapped frames	Mean red	X	OK	–	–	–
	Mean green	X	OK	–	–	–
	Mean blue	X	OK	–	–	–
	Mean *PC*1 (Fig. 17a and b)	OK	OK	958	922	950
(e)	Max *RGB*	OK	X	–	–	–
1 Hz	Mean gray	X	OK	–	–	–
	Mean red	X	OK	–	–	–
	Mean green	X	OK	–	–	–
	Mean blue	X	OK	–	–	–
	Mean *PC*1	OK	OK	1056	952	1010

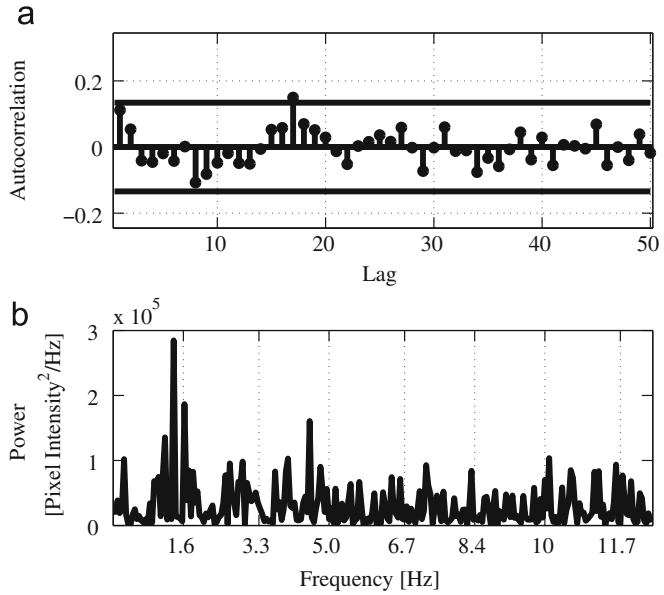

Fig. 15. Autocorrelation chart (a) and the frequency response plot (b) of the mean *PC*1 signal sampled at 25 Hz.

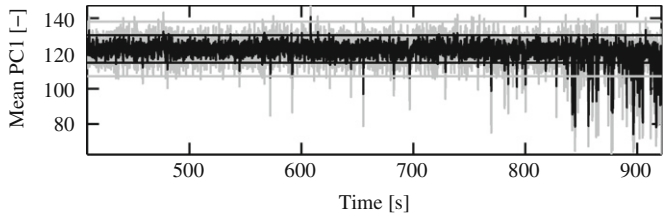

Fig. 16. Shewhart and EWMA control charts designed on the mean value of *PC*1 images sampled at 25 Hz.

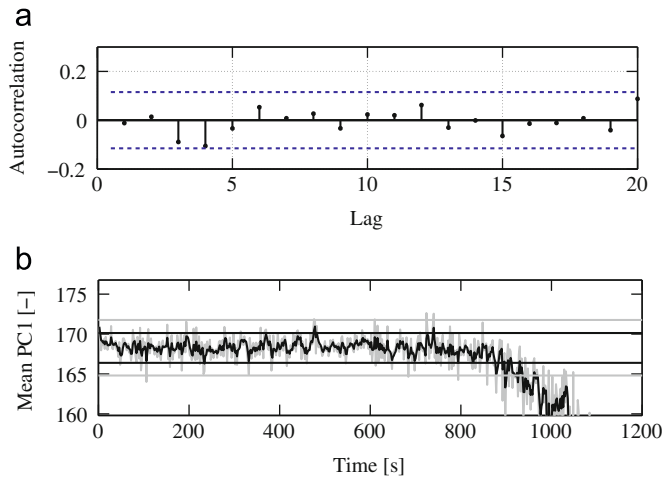

Fig. 17. Autocorrelation (a) and SPC chart (b) of the mean *PC*1 images sampled at 25 Hz with overlapping.

the mean gray intensity trends obtained using bulk video imaging requires the design of custom filters based on the frequency domain characteristics of the time series. In this case a filter is designed in the frequency domain and inverted using a fast Fourier transformation (FFT) to shift the filter in the time domain. The design of such digital filters is not subject of further investigation in this article.

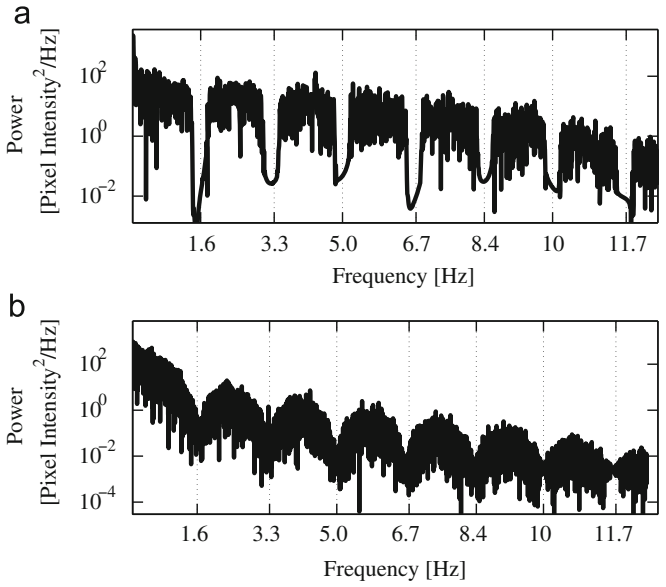

Fig. 18. Band-stop (a) and moving average (b) filtering result in the frequency domain of the mean gray intensity signal sampled at 25 Hz.

4.4. Acoustic signal monitoring results

At the beginning of the crystallization process, the sounds produced are monotone and upon nucleation onset a noticeable change occurs characterized by high pitched sounds. Monitoring the nucleation onset via acoustic inspection by human operators introduces a high degree of subjectivity since it heavily relies on the operators' acoustic memory. The main drawback of this approach is that it is difficult to have a comparison basis of the sound produced during nucleation in relation to the sound produced when the solution was clear. It is concluded that nucleation is detected only after a significant change in the sound pattern has occurred and it is less accurate than the other methods presented in this paper; nevertheless, its application could be evaluated for other process monitoring purposes.

5. Conclusions

In this work bulk video imaging data analysis and monitoring strategies have been evaluated in the form of multivariate image analysis, feature descriptors and statistical control charts. The fastest methods for nucleation onset detection were the monitoring in the principal score space and control chart based monitoring of the mean gray intensity of *PC*1 images sampled at 25 Hz. The application of SPCs may be hindered by the autocorrelated time series, which show oscillatory patterns due to light reflected from the stirrer; however, this can be considerably reduced by performing operations with the first principal component of a color image; alternative solutions are stacking of frames by the dominating frequency or designing custom digital filters to decrease the time series autocorrelation.

It was found that performing PCA calculations on multi-dimensional or multispectral information not only provides the combination of variables that explain most of the variance at a certain time instance but also decreases possible autocorrelation features of the resulting time series. Finally, it is concluded that the statistical control chart assisted monitoring provides a systematic and feasible framework for nucleation onset detection which can be easily transferred into industrial environments.

For acoustic signal based monitoring the gray scale images were converted into a 2 channel stereo sound. It was found that this method has less performant nucleation onset detection capabilities compared to the methods which directly rely on the images.

Nomenclature

A	number of principal components
B	blue component channel
Ch	color, gray, or principal component channel
E	residual matrix
F	filter value
f_c	cutoff frequency
fs	sampling frequency in [Hz]
f_r	frequency as a function of sampling rate
G	green component channel
GR	gray intensity of the RGB image
H	size of the filter Kernel
M	image width [pixels]
N	image height [pixels]
ng	sub-group size
p	loading vector or histogram bin value
$PC1$, $PC2$	principal components
R	red component channel
t_a	score vector
u	lag
U	unfolded multivariate image array
w	weight
x	pixel intensity value along a color channel
y	time series
W	moving window size
$\overline{Y}$	sample mean

Greek symbols

λ	EWMA memory factor [–]
γ	autocovariance function
ρ	autocorrelation

Indices

f	image
i	pixel along image height
j	pixel along image width
q	pixels

Abbreviations

CFA	color filter array
BVI	bulk video imaging
EWMA	exponentially weighted moving average
FBRM	focused beam reflectance measurement
MIA	multivariate Image Analysis
MPCA	multiway principal component analysis
MSZW	metastable zone width
PSD	particle size distribution
RGB	color image defined by the red, green, and blue color channels
SPC	statistical process control
SVD	singular value decomposition
UV/Vis	ultra violet–visible
Var	variance

Acknowledgements

The authors appreciate the comments provided by Professor J. MacGregor, McMaster University, Canada, on the multivariate image analysis based monitoring. The imaging hardware related discussions provided by Dr. Fred Hugen from IMIX (www.imix.nl), the Netherlands are greatly acknowledged.

Appendix A

Univariate process control charts have been proposed in the forms of Shewhart, cumulative sum (CUSUM) and EWMA charts. These charts differ from each other by applying different weighting to past data samples: e.g. the Shewhart chart weights only the last observation, the CUSUM chart assigns equal weights to all observations in a moving window, and the EWMA applies an exponentially decaying weighting (Hunter, 1986) according to Eq. (A.1):

$$y_{t+1} = \sum_{s=0}^{t} w_s y_s \tag{A.1}$$

where y_s is the observation at time t, y_{t+1} is the EWMA prediction and w_s are the weights

$$w_s = \lambda(1-\lambda)^{t-s} \tag{A.2}$$

where λ is the memory factor [–] which usually takes values between 0.15 and 0.4. To increase monitoring robustness, control charts are used in conjunction with control rules when the process presents occasional outliers, which should not trigger an out-of-control signal. Multivariate extensions of univariate charts, e.g. Hotelling chart and multivariate EWMA represent monitoring solutions when several parameters are considered (Macgregor and Kourti, 1995; Nomikos and MacGregor, 1995b). Whenever the signals show a high degree of correlation, SPC charts are built on the latent variables obtained after performing PCA.

The autocorrelation of a time series at lag k is unknown in practice but it can be estimated for a stationary process according to Eq. (A.3):

$$\rho_k = \frac{\gamma_k}{\gamma_0}, \quad k = 0,1,2,\ldots, \tag{A.3}$$

where γ_k is the autocovariance function defined as

$$\gamma_k = \frac{1}{N}\sum_{t=1}^{N-k}(y_t-\overline{y})(y_{t+k}-\overline{y}), \quad k = 0,1,2,\ldots \tag{A.4}$$

where Y is the time series and $\overline{Y}$ is the sample mean. The 95% confidence interval is defined by two standard deviation limits $\pm 2(Var(\rho_k^2))^{1/2}$ where Var is the variance of ρ_k assuming that the true autocorrelations beyond some lag u are zero (Box et al., 2008):

$$Var(\rho_k) \approx \frac{1}{N}(1+2(\rho_1^2+\cdots+\rho_u^2)), \quad u = k-1 \tag{A.5}$$

An alternative autocorrelation test is the Durbin–Watson test (Durbin and Watson, 1950). There are two accepted approaches to build control charts on significantly autocorrelated data as summarized by Lu and Reynolds (1999): adjustment of the control limits and the calculation of variance to account for autocorrelation. The alternative approach is to fit a time series model and then use the residuals for monitoring.

References

Anderson, J.E., Moore, S., Tarczynski, F., Walker, D., 2001. Determination of the onset of crystallization of N1-2-(thiazolyl)sulfanilamide (sulfathiazole) by UV–vis and calorimetry using an automated reaction platform; subsequent characterization of polymorphic forms using dispersive Raman Spectroscopy.

Spectrochimica Acta Part A: Molecular and Biomolecular Spectroscopy 57, 1793–1808.
Armingol, J.M., Otamendi, J., de la Escalera, A., Pastor, J.M., Rodriguez, F.J., 2003. Statistical pattern modeling in vision-based quality control systems. Journal of Intelligent & Robotic Systems 37, 321–336.
Bayer, B.E., 1976. Color imaging array. U.S. Patent 3,971,065.
Bharati, M.H., Liu, J.J., MacGregor, J.F., 2004. Image texture analysis: methods and comparisons. Chemometrics and Intelligent Laboratory Systems 72, 57–71.
Bharati, M.H., MacGregor, J.F., 1998. Multivariate image analysis for real-time process monitoring and control. Industrial & Engineering Chemistry Research 37, 4715–4724.
Bharati, M.H., MacGregor, J.F., Tropper, W., 2003. Softwood lumber grading through on-line multivariate image analysis techniques. Industrial & Engineering Chemistry Research 42, 5345–5353.
Box, G.E.P., Jenkins, G.M., Reinsel, G.C., 2008. Time Series Analysis 4th ed. John Wiley & Sons, Inc., Hoboken, NJ.
Braatz, R.D., 2002. Advanced control of crystallization processes. Annual Reviews in Control 26, 87–89.
Calderon De Anda, J., Wang, X.Z., Roberts, K.J., 2005. Multi-scale segmentation image analysis for the in-process monitoring of particle shape with batch crystallisers. Chemical Engineering Science 60, 1053–1065.
Darakis, E., Khanam, T., Rajendran, A., Kariwala, V., Naughton, T.J., Asundi, A.K., 2010. Microparticle characterization using digital holography. Chemical Engineering Science 65, 1037–1044.
De Anda, J.C., Wang, X.Z., Lai, X., Roberts, K.J., Jennings, K.H., Wilkinson, M.J., Watson, D., Roberts, D., 2005. Real-time product morphology monitoring in crystallization using imaging technique. AIChE Journal 51, 1406–1414.
de Juan, A., Maeder, M., Hancewicz, T., Tauler, R., 2005. Local rank analysis for exploratory spectroscopic image analysis. Fixed size image window-evolving factor analysis. Chemometrics and Intelligent Laboratory Systems 77, 64–74.
de Juan, A., Maeder, M., Hancewicz, T., Tauler, R., 2008. Use of local rank-based spatial information for resolution of spectroscopic images. Journal of Chemometrics 22, 291–298.
Dunn, K., 2007. Maccmia, 1.81. McMaster University, Canada.
Durbin, J., Watson, G.S., 1950. Testing for serial correlation in least squares regression .1. Biometrika 37, 409–428.
Eggers, J., Kempkes, M., Mazzotti, M., 2008. Measurement of size and shape distributions of particles through image analysis. Chemical Engineering Science 63, 5513–5521.
Facco, P., Bezzo, F., Barolo, M., Mukherjee, R., Romagnoli, J.A., 2009. Monitoring roughness and edge shape on semiconductors through multiresolution and multivariate image analysis. AIChE Journal 55, 1147–1160.
Fujiwara, M., Chow, P.S., Ma, D.L., Braatz, R.D., 2002. Paracetamol crystallization using laser backscattering and ATR-FTIR spectroscopy: metastability, agglomeration, and control. Crystal Growth & Design 2, 363–370.
Geladi, P., Isaksson, H., Lindqvist, L., Wold, S., Esbensen, K., 1989. Principal component analysis of multivariate images. Chemometrics and Intelligent Laboratory Systems 5, 209–220.
Gosselin, R., Rodrigue, D., Gonzalez-Nunez, R., Duchesne, C., 2009. Potential of hyperspectral imaging for quality control of polymer blend films. Industrial & Engineering Chemistry Research 48, 3033–3042.
Gurbuz, H., Ozdemir, B., 2003. Experimental determination of the metastable zone width of borax decahydrate by ultrasonic velocity measurement. Journal of Crystal Growth 252, 343–349.
Hunter, J.S., 1986. The exponentially weighted moving average. Journal of Quality Technology 18, 203–210.
Joung, O.J., Kim, Y.H., Fukui, K., 2005. Determination of metastable zone width in cooling crystallization with a Quartz Crystal Sensor. Sensors and Actuators, B: Chemical Sensors and Materials 105, 464–472.
Kawabata, K., Takahashi, M., Saitoh, K., Asama, H., Mishima, T., Sugahara, M., Miyano, M., 2006. Evaluation of crystalline objects in crystallizing protein droplets based on line-segment information in greyscale images. Acta Crystallographica Section D—Biological Crystallography 62, 239–245.
Kempkes, M., Darakis, E., Khanam, T., Rajendran, A., Kariwala, V., Mazzotti, M., Naughton, T.J., Asundi, A.K., 2009. Three dimensional digital holographic profiling of micro-fibers. Optics Express 17, 2938–2943.
Kempkes, M., Vetter, T., Mazzotti, M., 2010. Measurement of 3d particle size distributions by stereoscopic imaging. Chemical Engineering Science 65, 1362–1373.
Khanam, T., Darakis, E., Rajendran, A., Kariwala, V., Asundi, A.K., Naughton, T.J., 2008. On-Line Digital Holographic Measurement of Size and Shape of Microparticles for Crystallization Processes —Art. No. 71551k. Part 1–2.
Kumar, F.J., Moorthy, S.G., Jayaraman, D., Subramanian, C., 1996. Estimation of metastable zone width, interfacial energy and growth rates of ktiopo4 crystallizing from k6p4o13 flux by hot stage microscopy. Journal of Crystal Growth 160, 129–135.
Larsen, P.A., Rawlings, J.B., 2009. The potential of current high-resolution imaging-based particle size distribution measurements for crystallization monitoring. AIChE Journal 55, 896–905.
Larsen, P.A., Rawlings, J.B., Ferrier, N.J., 2006. An algorithm for analyzing noisy, in situ images of high-aspect-ratio crystals to monitor particle size distribution. Chemical Engineering Science 61, 5236–5248.
Larsen, P.A., Rawlings, J.B., Ferrier, N.J., 2007. Model-based object recognition to measure crystal size and shape distributions from in situ video images. Chemical Engineering Science 62, 1430–1441.
Lilliefors, H., 1967. On Kolmogorov–Smirnov test for normality with mean and variance unknown. Journal of the American Statistical Association 62, 399–402.
Liu, J.J., MacGregor, J.F., Duchesne, C., Bartolacci, G., 2005. Flotation froth monitoring using multiresolutional multivariate image analysis. Minerals Engineering 18, 65–76.
Loffelmann, M., Mersmann, A., 2002. How to measure supersaturation? Chemical Engineering Science 57 4301–4310.
Lu, C.W., Reynolds, M.R., 1999. Ewma control charts for monitoring the mean of autocorrelated processes. Journal of Quality Technology 31, 166–188.
Lyczko, N., Espitalier, F., Louisnard, O., Schwartzentruber, J., 2002. Effect of ultrasound on the induction time and the metastable zone widths of potassium sulphate. Chemical Engineering Journal 86, 233–241.
Macgregor, J.F., Kourti, T., 1995. Statistical process-control of multivariate processes. Control Engineering Practice 3, 403–414.
Marciniak, B., 2002. Density and ultrasonic velocity of undersaturated and supersaturated solutions of fluoranthene in trichloroethylene, and study of their metastable zone width. Journal of Crystal Growth 236, 347–356.
Nagy, Z.K., Chew, J.W., Fujiwara, M., Braatz, R.D., 2008. Comparative performance of concentration and temperature controlled batch crystallizations. Journal of Process Control 18, 399–407.
Nembhard, H.B., Ferrier, N.J., Osswald, T.A., Sanz-Uribe, J.R., 2003. An integrated model for statistical and vision monitoring in manufacturing transitions. Quality and Reliability Engineering International 19, 461–476.
Nomikos, P., MacGregor, J.F., 1994. Monitoring batch processes using multiway principal component analysis. AIChE Journal 40, 1361–1375.
Nomikos, P., MacGregor, J.F., 1995a. Multi-way partial least squares in monitoring batch processes. Chemometrics and Intelligent Laboratory Systems 30, 97–108.
Nomikos, P., MacGregor, J.F., 1995b. Multivariate Spc charts for monitoring batch processes. Technometrics 37, 41–59.
O'Grady, D., Barrett, M., Casey, E., Glennon, B., 2007. The effect of mixing on the metastable zone width and nucleation kinetics in the anti-solvent crystallization of benzoic acid. Chemical Engineering Research & Design 85, 945–952.
Oppenheim, A.V., Schafer, R.W., 2010. Discrete-Time Signal Processing 3rd ed. Prentice Hall, Upper Saddle River, NJ.
Parsons, A.R., Black, S.N., Colling, R., 2003. Automated measurement of metastable zones for pharmaceutical compounds. Chemical Engineering Research & Design 81, 700–704.
Pollanen, K., Hakkinen, A., Reinikainen, S.P., Rantanen, J., Minkkinen, P., 2006. Dynamic Pca-based Mspc charts for nucleation prediction in batch cooling crystallization processes. Chemometrics and Intelligent Laboratory Systems 84, 126–133.
Ramanath, R., Snyder, W.E., Bilbro, G.L., Sander, W.A., 2002. Demosacking methods for Bayer color arrays. Journal of Electronic Imaging 11, 306–315.
Rodionova, O.Y., Houmoller, L.P., Pomerantsev, A.L., Geladi, P., Burger, J., Dorofeyev, V.L., Arzamastsev, A.P., 2005. Nir spectrometry for counterfeit drug detection - a feasibility study. Analytica Chimica Acta 549, 151–158.
Sarkar, D., Doan, X.-T., Ying, Z., Srinivasan, R., 2009. In situ particle size estimation for crystallization processes by multivariate image analysis. Chemical Engineering Science 64, 9–19.
Simon, L.L., Hungerbuhler, K., 2010. Industrial batch dryer data mining using intelligent pattern classifiers: neural network, neuro-fuzzy and Takagi–Sugeno fuzzy models. Chemical Engineering Journal 157, 568–578.
Simon, L.L., Nagy, Z.K., Hungerbuhler, K., 2009a. Comparison of external bulk video imaging with focused beam reflectance and ultra violet-visible spectroscopy for crystallization nucleation detection and metastable zone identification. Chemical Engineering Science 64, 3344–3351.
Simon, L.L., Nagy, Z.K., Hungerbuhler, K., 2009b. Endoscopy-based in situ bulk video imaging of batch crystallization processes. Organic Process Research & Development, Special Issue on Polymorphism and Crystallization 13, 1254–1261.
Sohnel, O., Mullin, J.W., 1988. The role of time in metastable zone width determinations. Chemical Engineering Research & Design 66, 537–540.
Szatvanyi, G., Duchesne, C., Bartolacci, G., 2006. Multivariate image analysis of flames for product quality and combustion control in rotary kilns. Industrial & Engineering Chemistry Research 45, 4706–4715.
Tessier, J., Duchesne, C., Bartolacci, G., 2007. A machine vision approach to on-line estimation of run-of-mine ore composition on Conveyor belts. Minerals Engineering 20, 1129–1144.
Tessier, J., Duchesne, C., Gauthier, C., Dufour, G., 2008. Estimation of alumina content of anode cover materials using multivariate image analysis techniques. Chemical Engineering Science 63, 1370–1380.
The Mathworks, I., (2008) Matlab, 7.6.0.324 (R2008a), the Mathworks, Inc, Natick, MA, USA 〈www.Mathworks.Com〉.
Tomba, E., Facco, P., Roso, M., Modesti, M., Bezzo, F., Barolo, M., 2010. Artificial vision system for the automatic measurement of interfiber pore characteristics and fiber diameter distribution in nanofiber assemblies. Industrial & Engineering Chemistry Research 49, 2957–2968.
Wang, Y.Q., Gao, F.R., Doyle, F.J., 2009. Survey on iterative learning control, repetitive control, and run-to-run control. Journal of Process Control 19, 1589–1600.
Yu, H.L., MacGregor, J.F., 2003. Multivariate image analysis and regression for prediction of coating content and distribution in the production of snack foods. Chemometrics and Intelligent Laboratory Systems 67, 125–144.
Yu, H.L., MacGregor, J.F., 2004. Monitoring flames in an industrial boiler using multivariate image analysis. AIChE Journal 50, 1474–1483.
Yu, H.L., MacGregor, J.F., Haarsma, G., Bourg, W., 2003. Digital imaging for online monitoring and control of industrial snack food processes. Industrial & Engineering Chemistry Research 42, 3036–3044.
Zhou, Y., Srinivasan, R., Lakshminarayanan, S., 2009. Critical evaluation of image processing approaches for real-time crystal size measurements. Computers & Chemical Engineering 33, 1022–1035.